Structural organization of Weibel-Palade bodies revealed by cryo-EM of vitrified endothelial cells

John A. Berriman[a,1], Sam Li[b,2], Lindsay J. Hewlett[c], Sebastian Wasilewski[a], Fedir N. Kiskin[a], Tom Carter[c], Matthew J. Hannah[c], and Peter B. Rosenthal[a,3]

[a]Divisions of Physical Biochemistry and [c]Molecular Neuroendocrinology, MRC National Institute for Medical Research, The Ridgeway, Mill Hill, London, NW7 1AA, United Kingdom; and [b]Division of Cell Biology, MRC Laboratory of Molecular Biology, Hills Road, Cambridge, CB2 0QH, United Kingdom

Edited by Wolfgang Baumeister, Max Planck Institute of Biochemistry, Martinsried, Germany, and accepted by the Editorial Board August 18, 2009 (received for review March 27, 2009)

In endothelial cells, the multifunctional blood glycoprotein von Willebrand Factor (VWF) is stored for rapid exocytic release in specialized secretory granules called Weibel-Palade bodies (WPBs). Electron cryomicroscopy at the thin periphery of whole, vitrified human umbilical vein endothelial cells (HUVECs) is used to directly image WPBs and their interaction with a 3D network of closely apposed membranous organelles, membrane tubules, and filaments. Fourier analysis of images and tomographic reconstruction show that VWF is packaged as a helix in WPBs. The helical signature of VWF tubules is used to identify VWF-containing organelles and characterize their paracrystalline order in low dose images. We build a 3D model of a WPB in which individual VWF helices can bend, but in which the paracrystalline packing of VWF tubules, closely wrapped by the WPB membrane, is associated with the rod-like morphology of the granules.

electron cryomicroscopy | paracrystal | von Willebrand factor | tomography

Endothelial cells line the inner surfaces of blood vessels and play important roles in hemostasis, thrombosis, and inflammation. Some of these roles are achieved by secretion of the large, multimeric blood glycoprotein von Willebrand factor (VWF). VWF has multiple ligands and on acute release functions as an adhesive protein to bind platelets to sites of vascular injury. VWF circulating in the bloodstream also functions as a carrier for coagulation Factor VIII, increasing its lifetime. Defects in VWF and its storage are responsible for bleeding disorders including von Willebrand's disease (1).

VWF is synthesized as a 350-kDa precursor (proVWF) that forms disulfide-linked dimers in the ER through its C-terminal cysteine knot domain. Proteolytic cleavage of proVWF in the Golgi gives rise to the N-terminal propolypeptide (a 100-kDa protein called proregion) and to mature VWF dimers that form large homo-oligomers through disulfide-links near each of its mature N-termini, a process catalyzed by proregion (2, 3). VWF and proregion remain non-covalently associated and are stored together in specialized secretory organelles called Weibel-Palade bodies (WPBs), first identified by EM of fixed tissue sections as rod-shaped organelles containing fine tubules (4). Secretagogues stimulate WPB exocytosis, releasing VWF and other low molecular weight molecules such as cytokines and chemokines into the bloodstream (5), although mature VWF and its proregion account for greater than 95% of the protein in the granule (6). On release, VWF multimers are able to unfurl to strings up to 100 μm long and associate with multiple ligands on platelet and endothelial cell surfaces at the site of vascular injury to help form a platelet plug. Mechanical shear exposes ligand binding sites on VWF as well as sites for cleavage by the protease ADAMTS13, which regulates the length of VWF multimers in the bloodstream (7).

Like most other secretory granules, WPBs are thought to form at the trans-Golgi network (TGN) in a pH-dependent process. P-selectin is also recruited to the WPB membrane at the TGN (8) and functions in leukocyte recruitment after delivery to the endothelial cell surface by WPB exocytosis. Maturation of WPBs is marked by the recruitment of the membrane-associated GTPases Rab27a (9) and Rab3D (10) and the membrane tetraspanin CD63 (8, 11). Exogenous expression of VWF leads to the de novo formation of WPBs in a number of non-endothelial mammalian cell lines (12). This suggests that VWF drives the formation of WPBs and makes WPBs an attractive system for studies of organelle formation within the secretory pathway.

Electron cryotomography can provide a significant advance in the understanding of cellular interactions by directly imaging the complex 3D organization of the cell (13–15). Cell thickness is a limiting factor in such investigations, and studies have used small cells (16, 17), the edge of frozen-hydrated cells (18–20), or vitreous sections (21, 22). Here we report electron cryomicroscopy of whole-mount human umbilical vein endothelial cells (HUVECs) that are vitrified by rapid plunge-freezing, providing an outstanding view of WPBs and their surrounding architecture at the thin edge of the cell without the fixation, dehydration, embedding, staining, and sectioning used in earlier studies employing conventional plastic sections (23) or high pressure freezing/freeze substitution (24). The images represent an advance because the contrast results from the cellular structures themselves and not from stain distributions. Because the cells are un-sectioned, we are able to build 3D models for WPBs in close apposition with other membranous organelles and a network of membrane tubules and protein filaments. We address structural aspects of two problems posed by VWF trafficking: how can a long multimeric protein be organized for dense storage in WPBs, and how can the packaging of this protein determine the identity and morphology of this unique secretory granule? We combine images and tomograms to show that VWF is packaged as a helix in WPBs similar to those that can be assembled in vitro from only proregion (domains D1D2) and the N-terminal D'D3 domains of mature VWF (25). We build a 3D model describing the higher-order assembly of VWF tubules and the surrounding membrane in a WPB.

Results and Discussion

Cryomicroscopy of Frozen-Hydrated HUVECs. HUVECs grown on carbon-coated gold grids were observed by light microscopy to

Author contributions: J.A.B., T.C., M.J.H., and P.B.R. designed research; J.A.B., S.L., L.J.H., F.N.K., T.C., and P.B.R. performed research; S.W. contributed new reagents/analytic tools; J.A.B., S.L., S.W., T.C., and P.B.R. analyzed data; and P.B.R. wrote the paper.

The authors declare no conflict of interest.

This article is a PNAS Direct Submission. W.B. is a guest editor invited by the Editorial Board.

[1]Present address: 51 Oakhill Road, Putney, SW15 2QJ, United Kingdom.

[2]Present address: Department of Biochemistry & Biophysics, University of California at San Francisco, 600, 16th Street, San Francisco, CA 94158.

[3]To whom correspondence should be addressed. E-mail: peter.rosenthal@nimr.mrc.ac.uk.

This article contains supporting information online at www.pnas.org/cgi/content/full/0902977106/DCSupplemental.

CELL BIOLOGY

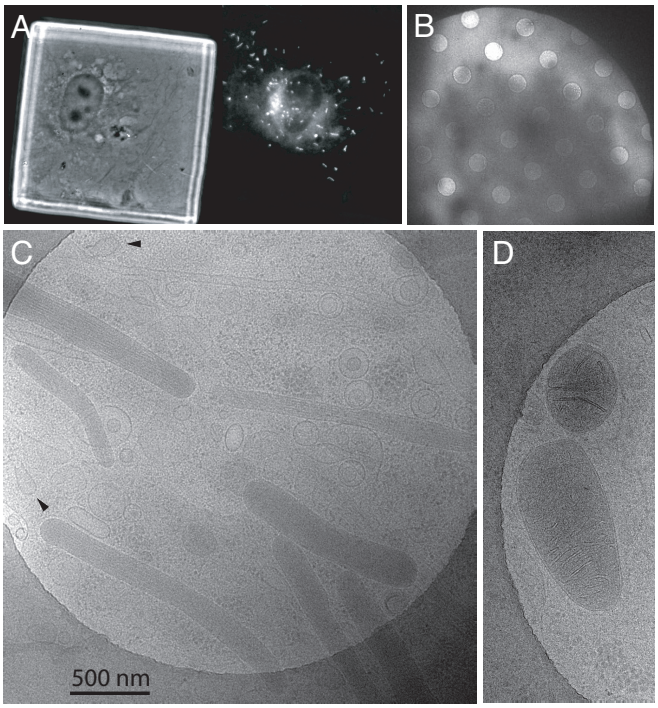

Fig. 1. Endothelial cells grown on carbon-coated electron microscope grids. (*A*) Phase contrast (left) and fluorescent (right) images of grid square with HUVEC expressing EGFP-hRab27a showing WPBs. (*B*) Low magnification image of the electron-transparent edge of a cell extending over holes in the carbon film. (*C*) Image of the edge of a frozen-hydrated cell showing several WPBs and arrows pointing to membrane invaginations. (*D*) Two mitochondria.

flatten, sometimes over areas larger than the 60-μm grid square, and contain WPBs, as shown by fluorescent rod-shapes in cells transiently expressing EGFP-Rab27a (Fig. 1*A*), a marker for mature WPBs (9). Images of whole, plunge-frozen HUVECs were recorded by low dose cryomicroscopy at liquid nitrogen temperature using 120 keV or 300 keV electrons. Thick parts of cells were opaque to electrons, but cells were transparent toward the periphery (Fig. 1*B*). We used a strategy of recording low dose images (30,000× magnification, incident dose $<4\ e^{-}/Å^2$) (26) for high resolution analysis followed by a tilt series for electron tomographic reconstruction (15,000× magnification, total dose $<50\ e^{-}/Å^2$) (27) to study features in 3D without overlap. These were recorded at locations within the cell periphery that had a thickness of approximately 0.1–0.3 μm, values determined by the fractional scattering of electrons by the specimen (Fig. S1) and confirmed in measurements on reconstructed 3D volumes. These revealed a densely packed environment of organelles including mitochondria, multivesicular bodies, coated vesicles, caveolae, and WPBs.

The success in imaging HUVEC architecture is in part due to its thinness, which provides a shorter depth for electrons to penetrate, and allows rapid cooling to a vitreous state, avoiding ice formation which damages cell structure. A wide range of structures were observed using 120 keV electrons without an energy filter. Studies aimed at thicker parts of the specimen may require higher voltage electrons with energy filtration (27, 28). Overexposure during a dose series (Fig. S2) or a tilt series ($>50\ e^{-}/Å^2$) (Movie S1), caused a selective bubbling (16, 17) of the internal contents of WPBs compared to other organelles and cell structures. Because some carbohydrates have been shown to promote bubbling (29), we suggest that this radiation damage effect may be attributed to the extensive glycosylation of the VWF glycoprotein (>15% by weight) (30) combined with its density in the granule.

Fig. 1*C* shows an image of several WPBs observed in the periphery of the cell over a hole in carbon. They are immediately recognizable by their rod-like shape, homogeneous density (≈10% greater scatter than cytoplasm, Fig. S1), and presence of tubular striations running along the long axis of the body, which lies in the plane of the cell. By comparison a mitochondrion, another dense organelle, is readily identified by its double outer membrane and cristae (Fig. 1*D*).

The WPBs observed in this study exclusively show a smooth membrane tightly surrounding the tubular contents. This is markedly different from the wavy membranes observed for WPBs in a previous study (23). Under defocus conditions where maximum phase contrast allows us to resolve the bilayer (spacing ≈4 nm), these WPB membranes are devoid of a protein coat, although we can detect these reliably on other vesicles (see movies and images below, e.g., Fig. 5*D*). Clathrin coats have been reported on nascent granules emerging from the TGN (24, 31). Immature granules lacking the membrane marker Rab27a are a small percentage of WPBs (9, 32) and are present near Golgi structures and not at the cell periphery. Our images at the cell periphery therefore show mature WPBs. An implication of the close wrapping of the granule content is that these WPBs are stable with respect to content and morphology: there is no extraneous space at the mature granule membrane for the granule to function as a vesicle donor, and similarly, we would expect to see extraneous space in granules that were receiving new membrane or undergoing homotypic fusion.

A tomogram (Movie S2; slice in Fig. 2) shows two WPBs (labeled Body A and Body B) embedded in a network of cytoskeletal filaments, microtubules, and ribosome-sized densities (Fig. S3). The preservation of membrane interactions is striking and in 3D we observe membranes connected by thin tubules and membranes exhibiting sharp corners, morphological features that result from membranes interacting with filaments. The WPBs are in close association with other membranous organelles and membrane tubules. Body A interacts with "bouton-shaped" organelles (dark blue in the model derived from segmentation of the tomogram in Movie S3), the membranes of which flatten at the point of contact with the right side of the "club" end of this granule (labeled by an asterisk) and form what may be described as inter-organelle synapses. Another bouton to the left of the club extends into a network of membrane tubules wrapped by protein filaments.

Four multivesicular bodies (MVBs) are present in Fig. 2. The organelle at extreme right contains a small number of internal vesicles typical of an early endosomal multivesicular body (33). Body B is between two MVBs, and the membrane of one of the MVBs flattens against the WPB at the point of contact, also forming a synapse-like structure, with protein density connecting the membranes. This association is much closer than the tethering observed in plastic section between multivesicular endosomes and lysosomes (34). These MVBs contain many more internal vesicles and a denser content, identifying them as a late endosomal/lysosomal compartment. The MVB to the right contains an internal membrane surrounded by an electron lucent space, although the internal membrane has been partially degraded and consists of blunt membrane pieces. These features are typical of an autophagic compartment (35), and indeed, the particles in the inner compartment seem very similar in size and density to that observed in the surrounding cytoplasm. Physical association of MVBs and WPBs is consistent with known cross-talk between late endosomal compartments and WPBs. The lysosomal protein CD63 is also a marker for WPBs, but the majority of cellular CD63 resides in the internal vesicles of MVBs (8, 11). Some integral membrane proteins are recycled from endosomal compartments to the TGN where they are incorpo-

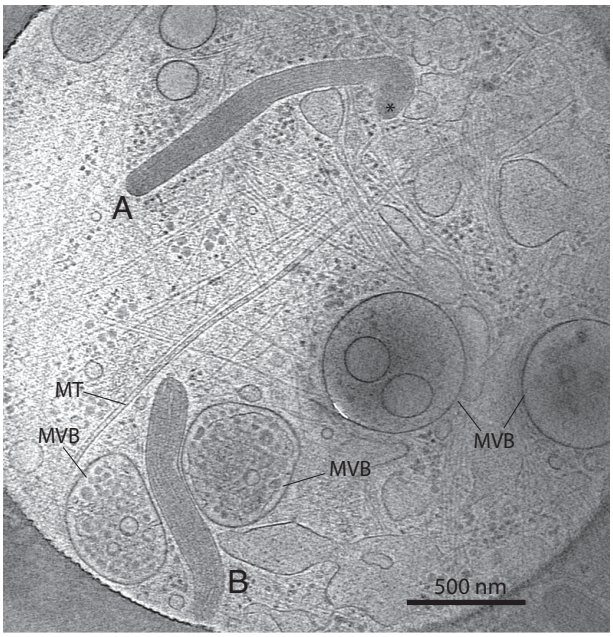

Fig. 2. Tomogram (Movie S2) section shows cell periphery with WPBs (Body A and Body B, club-end noted by asterisk), microtubule (MT), and MVBs.

rated into nascent granules. In the case of CD63, there may also be a direct transfer from MVBs to WPBs (8, 11).

Multimeric Von Willebrand Factor Tubules Are Helical and Form a Paracrystal in Weibel-Palade Bodies. Fig. 3 *A* and *B* shows sections of the tomogram of Body B in Fig. 2 with VWF tubules. VWF tubules are in close contact, so that the largest density gaps in the WPB are in the interior of the tubules and not between the tubules, and are closer than previously observed in plastic sections (23). The tubules have an inner diameter of about 120 Å and an outer diameter of about 240 Å. They have a periodic arrangement of mass at high radius that in some cases shows further extensions toward adjacent tubules. The periodic arrangement of densities on the tubules in tomograms appears to be helical. To visualize higher-resolution features of the tubules than present in the tomograms, individual, non-overlapped VWF tubules were identified at the edge of WPBs in single low dose images recorded at 120 keV and 300 keV. As shown in Fig. 3*D* and Fig. S4, these are similar to the tubules in the tomograms. Image analysis (Fourier transformation) shows them to have a helical organization with a very strong third layer line at 120 Å (Fig. 3*F*). The repetitive structure is enhanced after filtering the Fourier transform (Fig. 3*E*).

The molecular structure of the VWF tubules was next studied by image analysis of entire granules. For all bodies tested, the prominent 120-Å repeat is a consistent feature oriented along the main axis of the granule and reorienting across hinges. Often in bodies that deviate from a rod-shape (e.g., Fig. S4), the transform confirms regions of poor tubule alignment. We conclude that this Fourier transform is the unique molecular signature of VWF tubules in the cell images.

Fig. 4*A* shows a WPB with an ordered, straight domain, and its Fourier transform in Fig. 4*B* shows a peak on the meridian at 27.7 Å, evidence of high resolution structure preservation in frozen-hydrated preparations. The pattern arises from a precise parallel alignment of the VWF tubules in a paracrystal. The lattice drawn on half the pattern in Fig. 4*B* shows that the VWF tubules are helices with a repeat of 360 Å in which 13 subunits make three turns (≈4.3 subunits per turn). A model for the VWF

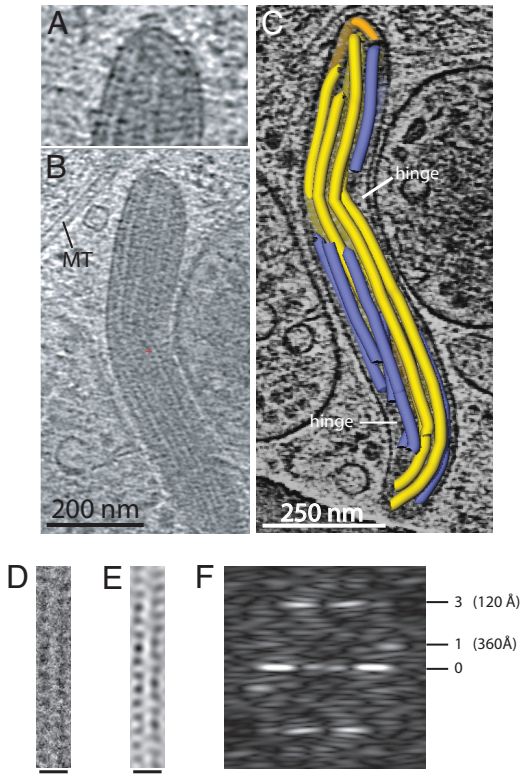

Fig. 3. Tomogram sections and images showing VWF tubules. (*A*) Section of tomogram (after 18° rotation of tomogram about an axis along the granule) shows a VWF tubule closely following the membrane and buckling at the granule end. (*B*) A 100-Å thick projected tomogram section from Body B showing VWF tubules and a microtubule (MT). (*C*) Structural model for VWF tubules. Tubules running full-length of the granule in yellow (one bending at the granule end is orange), shorter tubules in blue, hinges indicated. (*D*) VWF tubule from the edge of an irregular WPB recorded at 300 keV in Fig. S4*B* before and (*E*) after Fourier filtering to include only the equator and layer lines 1 and 3 in the Fourier transform (*F*) of the tubule in (*D*). [Scale bar, 250 Å in (*D* and *E*).]

tubule (Fig. 4*C*) is obtained by applying the helical symmetry identified in the paracrystal to the image of the single filament projection in Fig. 3*E*. The model of the VWF tubule in frozen-hydrated WPBs has a corrugated wall with large fenestrations. An end-on view of the model is compared with a VWF tubule end-on view (Fig. 4*D*) occasionally observed in WPBs of irregular shape.

The model is very similar to a structure obtained from negative stain images of tubules assembled in vitro from only the D1D2/D'D3 domains (See sequence diagram in Fig. 4*E*) under low pH and divalent calcium conditions similar to those present during VWF assembly in the TGN (25). The repeating subunit of the in vitro structure has been interpreted as consisting of a covalent D'D3 domain dimer and two proregions (D1D2). Full length VWF in WPBs therefore forms the same core helix but decorated by the additional 55% of the VWF full-length polypeptide. Three VWF A repeats and the D4 domain (together 35% of the VWF polypeptide) immediately follow D'D3 in sequence and likely account for the density seen at high radius in some tubule images and may explain arms reaching between VWF tubules (Fig. 3 *A* and *B*). Highly extended C-terminal polypeptides, disulfide-linked at a cysteine knot (CK) domain, connect the repeating subunits of the core helix (25) but are likely poorly ordered. Multimerization is required for VWF function following release by exocytosis although not for tubule (25) or granule formation (36). Disassembly of the helix during

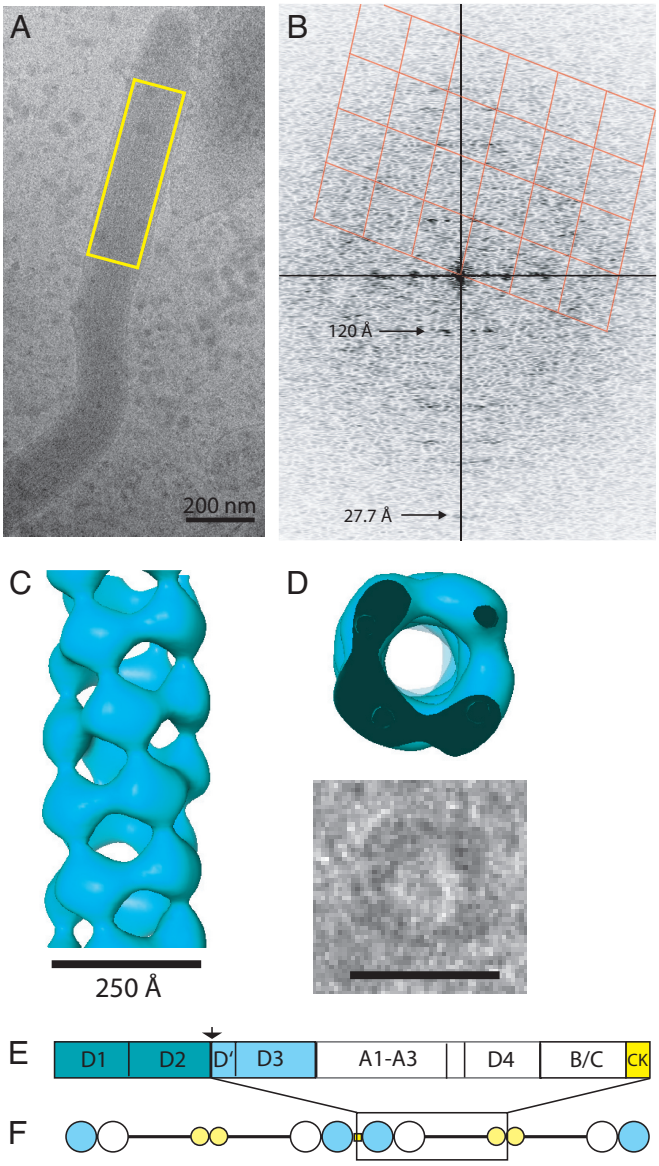

Fig. 4. WPBs are paracrystalline assemblies of helical VWF tubules. (*A*) WPB with box over paracrystalline region used to calculate the Fourier transform in (*B*) with helical lattice in red and layer line 3 at 120 Å and layer line 13 at 27.7 Å (meridional) indicated with arrows. (*C*) VWF tubule model side-view. (*D*) Model end-on view compared with image of a tubule seen end-on. (Scale bar, 250 Å.) (*E*) VWF domain diagram, with those forming in vitro tubules in reference (25) in blue and arrow at proregion cleavage site. (*F*) Schematic for mature VWF multimers.

granule exocytosis would then produce mature, multimeric VWF with globular domains separated by more extended polypeptide giving the appearance of beads on a string (schematic, Fig. 4*F*) as in rotary shadowing images (37).

In contrast to the in vitro tubules, which appear to be flexible and display a large variation in helical pitch, the helical signature of WPBs in vitrified endothelial cells shows a more consistent pitch near 120 Å. While variability may be an effect of negative stain, the consistency in WPBs may arise from a greater regularity or rigidity of the tubules composed of full-length VWF or from constraints on the tubules in the context of the paracrystalline assembly. The corrugated structure of the VWF tubules may facilitate alignment in the paracrystal. VWF domains that are not part of the core helix may play other roles in WPB structure or formation including forming cross-bridges between tubules, and interacting with the membrane or with membrane-associated proteins such as P-selectin (38).

3D Model for a Weibel-Palade Body. Electron cryotomography reveals the 3D packing organization of the VWF tubules within the membrane of a complete WPB. A structural model for the WPB Body B of Fig. 2 is shown in Fig. 3*C* and Fig. S5, and is superimposed on the tomogram (Movie S4). The path of the tubules was determined by cross-correlation of the VWF helix density against the tomogram. The model consists of fourteen tubules, five of which run approximately the full-length of the granule but kink at two hinges in the body. The other nine tubules are shorter and are confined to either side of the hinge. Most tubules are slightly deformed near their ends. The mean distance calculated between a point at the center of each tubule and that of its nearest neighbor is 284 ± 31.3Å (Fig. S5) indicating near close-packing of helical tubules. Individual tubules at the edge of the paracrystal follow the shape of the membrane and pack as closely to the membrane as they do to adjacent tubules (Fig. S5). The rod shape of the organelle membrane is therefore associated with the shape of the paracrystal.

Bending of tubules at the ends of granules (Fig. 3*A* and Figs. S4 and S5) is an important feature of the images and indicates that the tubules are flexible. Flexible tubules with ends extending outside the paracrystalline core are observed to curve or buckle to accommodate the membrane curvature at the end of granules. The paracrystalline assembly of tubules is therefore stiffer than individual tubules and determines the shape of the surrounding membrane against which the tubules pack closely. This is similar to observations of other fibril assemblies that determine the shape of membranes (39).

Although some WPBs are straight, others show hinges. Hinges rely on the concerted kinking of flexible tubules between straight paracrystalline regions (Fig. 3*C* and Fig. S5). This is typical of other flexible, corrugated polymers that align in a paracrystal, where the energetic cost of bending the whole assembly is greater than introducing a local kink that otherwise maintains normal packing or interdigitation (39). Kinks may also preserve paracrystalline interactions while accommodating defects such as broken or shortened tubules. The kinking of tubules at the hinges is associated with both positive and negative curvature in the surrounding membrane. At the points of greatest negative membrane curvature, which occur at the two hinges in Body B (Fig. 3*C*) and near the club-feature in Body A in Fig. 2, the tubules fail to follow the membrane and voids occur. This also suggests that the morphology of the membrane is determined by the rigidity of the paracrystalline assembly of tubules.

A Weibel-Palade Body Associated with the Plasma Membrane. Identification of a particular protein or structural feature in the crowded environment of the cell is challenging for electron cryomicroscopy. Our ability to detect the molecular signature of VWF in low contrast images should allow us to follow the transport of VWF tubules through accessible parts of the secretory pathway, or to associate the disruption of paracrystallinity with disease-causing mutations in VWF.

The image in Fig. 5*A* and tomogram section in Fig. 5*D* (also tomogram in Movie S5) shows a marrow-shaped granule quite different from the typical rod-shaped WPBs presented in earlier figures. Nevertheless, the granule shows the molecular signature (Fig. 5*B*) of VWF identifying it as a WPB. The VWF paracrystal appears to be disassembling, with VWF tubules bowed outward from the axis and with greater separation between tubules. The typical layer lines appear as arcs in Fig. 5*B* reflecting the disorder. Most striking in Fig. 5*D* is a membranous connection between the tip of the granule and the plasma membrane. In the projection shown, the connection is 270 Å at its widest and it tapers as it reaches the tip of the granule where the granule membrane inverts

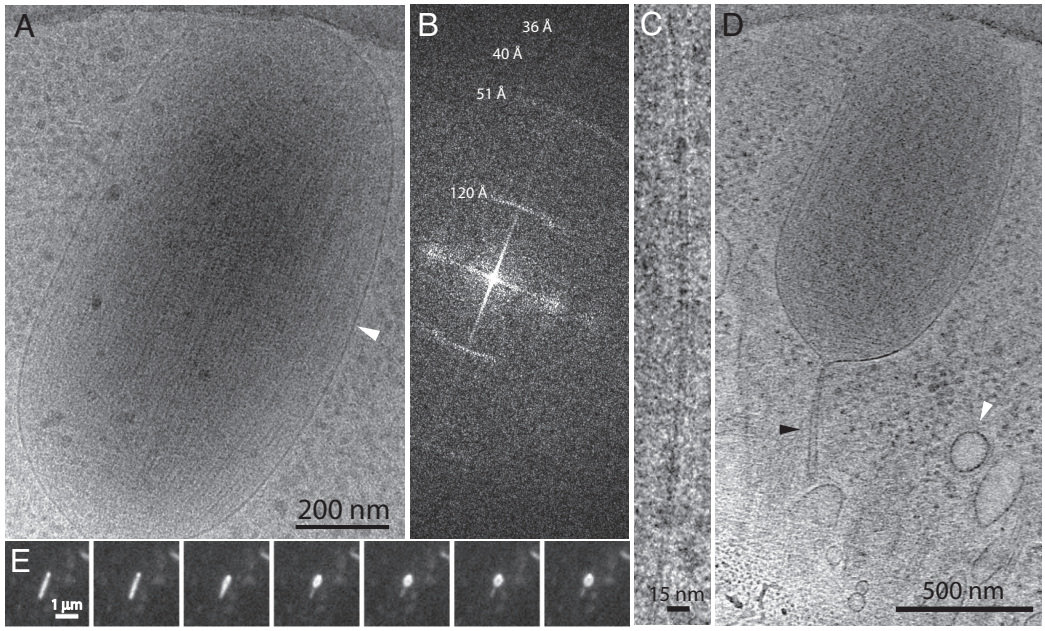

Fig. 5. Marrow-shaped granule near plasma membrane. (*A*) Image over a hole in ice, defocus = 4.6 μm. (*B*) Fourier transform of granule content shows layer lines typical of helical VWF. (*C*) Image of membrane bilayer located at white arrow on granule in (*A*), defocus = 2 μm. (*D*) Projection of tomogram sections (see Movie S5) shows a thin structure (black arrow) connecting the granule to the plasma membrane. A coated vesicle is also shown (white arrow). (*E*) Montage of EGFP-CD63 fluorescence microscopy images of a WPB during histamine-evoked fusion of WPBs (Movies S6 and S7).

curvature. VWF tubules are also oriented orthogonal to the main axis of the body near the tip of the granule.

We imaged cells transiently expressing the membrane marker EGFP-CD63 by fluorescence microscopy to observe changes in WPB morphology during histamine-evoked exocytosis. Exocytosis of WPBs often revealed a thin projection of WPB-derived membrane extending from the rounded or marrow-shaped structures (formed following fusion; references (5, 40)) to the plasma membrane (Fig. 5*E* and Movies S6 and S7). The EM images in Fig. 5 show granule morphology consistent with granule swelling driven by membrane fusion at the plasma membrane that causes a pH elevation and partial hydration of the granule core (40). The morphology change is associated with a loss of alignment in the VWF paracrystal.

A Structural Model for WPB Formation. The structural organization of VWF in WPBs suggests a specific model by which VWF can drive formation of a granule. VWF is organized as a helix in WPBs, similar in structure to helices formed by assembly of the D1D2/D'D3 domains of VWF in vitro (25). Covalent addition of a new VWF dimer to the end of a growing helix, catalyzed by proregion, provides a strategy for packaging the long strings of covalently-linked VWF without entanglement. Images and tomograms identify the close packing of VWF tubules in the paracrystal as the most important feature of granule architecture. Immature granules likely form through the retention and aggregation of helical VWF that is too large to be sorted into small transport vesicles at the TGN. Selective retention of VWF in the granule occurs as membrane and non-VWF content leave the granule by vesicle budding (41), although granules could increase in size and VWF content by homotypic fusion events. The dense paracrystalline core resulting from the alignment of VWF tubules, because of its stability against further sorting or dispersal, may be sufficient to give the granule a unique shape and content. The mature granule membrane is wrapped tightly around the paracrystal and lacks a coat. Higher-resolution studies will be required to address whether the paracrystal may also function as a scaffold that organizes or retains proteins such as P-selectin (38) or lipids of the surrounding membrane (42), giving the granule a unique identity in the secretory pathway.

Materials and Methods

Growth of HUVECs on Carbon Films. Primary HUVECs were purchased from TCS Cellworks and grown as previously described (43) except endothelial cell growth supplement was purchased from Upstate . Cells were trypsinized (in some cases Nucleofected, see below), re-suspended in growth medium, and transferred to tissue culture dishes (Nunc) at subconfluent density. Immediately following this, carbon coated microscopy grids or 300 mesh gold Quantifoil™ grids (R3/3) with an additional thin layer of carbon and glow discharged, were placed into the growth medium. Cells were grown overnight at 37 °C, 5% CO_2 before electron microscopy.

Electron Cryomicroscopy. Grids supporting cell growth were removed from the cell culture medium using tweezers, were dipped in a vial of PBS (Dulbecco's, Invitrogen), preblotted with filter paper, then transferred to the environment chamber (4 °C, 90% R.H.) of a Vitrobot Mark III (FEI) and blotted on both sides with a double layer of paper for 10 s before plunging into liquid ethane. Grids were transferred to a Gatan 626 tomography holder or Polara stage. Imaging was performed in an FEI Spirit TWIN microscope at 120 keV using a tungsten filament source and equipped with a cryobox around the sample. Images were recorded un-binned on an Eagle 2K camera (FEI) at 15 K magnification (13.8 Å/pixel) for tomography or 30 K magnification (7.2 Å/pixel) for single images under low dose conditions. Magnification was calibrated by recording images of tobacco mosaic virus (courtesy of Ruben Diaz-Avalos, New York Structural Biology Center) under identical conditions. Tilt series for tomography were recorded manually with 6–8 μm under-focus as a succession of low dose images tilted from 0 to $\pm$ 60° in 4° steps with a total dose less than 50 $e^{-}/Å^2$. An FEI G2 Polara operating at liquid nitrogen temperature and 300 keV was used to collect images and tilt series on a 224HD detector (TVIPS) giving a 9.1 Å pixel at 15 K magnification.

Image and Tilt Series Analysis. Tomographic tilt series were aligned using IMOD software (44). Alignment initially used cross correlation and then used available dense features as fiducials. The projection images in the aligned tilt series were normalized based on their histograms using Bsoft (45) and the final reconstructed 3D volume was generated by an iterative alignment and reconstruction procedure using the Priism package (46). Images were analyzed using FFTRANS and Ximdisp programs from the MRC package (47). A model for the VWF tubule (Fig. 4 *C* and *D*) was computed using Spider Software (48) by cutting the Fourier-

filtered filament image into segments along the helical axis (49), computing a 3D volume by assigning segments separated ΔZ along the filament axis a relative angle $\phi = (\Delta Z/27.7\text{Å})(83.1°)$ to impose the helical selection rule ($l = 3n + 13m$), further enforcing symmetry with himpose (50), and assigning the same absolute hand as described for D1D2/D'D3 tubules (25). Segmentation of tomographic volumes was performed by drawing contours manually on sections with the segmentation editor and edge detection facility of Amira (Visage Imaging). The path of the VWF tubules within the WPB was determined by a search of the helical model of the tubule against the masked WPB using a 2D template matching procedure implemented in Matlab (Mathworks) and further details are given in *SI Text* and Fig. S5.

Bright Field and Fluorescence Microscopy. Human Rab27a cDNA (gift from Guthrie cDNA resource centre www.cdna.org) was cloned into pEGFP-C3 (Clontech) using *Hin*dIII/*Apa*I. For fixed cell imaging, grids supporting cells Nucleofected with EGFP-hRab27a were fixed, mounted and imaged as previously described (51). For live-cell fluorescence microscopy, cells expressing EGFP-CD63 were imaged at 7 frames per s during histamine (100 μM) stimulation at 37 °C as previously described (5) and data analyzed in ImageJ Software (http://rsb.info.nih.gov/ij).

ACKNOWLEDGMENTS. This work was funded by the Medical Research Council (U.K.). F.N.K. was recipient of a Nuffield Bursary Fellowship.

1. Sadler JE (1998) Biochemistry and genetics of von Willebrand factor. *Annu Rev Biochem* 67:395–424.
2. Purvis AR, et al. (2007) Two Cys residues essential for Von Willebrand factor multimer assembly in the Golgi. *Proc Natl Acad Sci USA* 104:15647–15652.
3. Purvis AR, Sadler JE (2004) A covalent oxidoreductase intermediate in propeptide-dependent von Willebrand factor multimerization. *J Biol Chem* 279:49982–49988.
4. Weibel ER, Palade GE (1964) New cytoplasmic components in arterial endothelia. *J Cell Biol* 23:101–112.
5. Babich V, et al. (2008) Selective release of molecules from Weibel-Palade bodies during a lingering kiss. *Blood* 111:5282–5290.
6. Ewenstein BM, Warhol MJ, Handin RI, Pober JS (1987) Composition of the Von Willebrand-factor storage organelle (Weibel-Palade body) isolated from cultured human umbilical vein endothelial cells. *J Cell Biol* 104:1423–1433.
7. Zhang X, Halvorsen K, Zhang CZ, Wong WP, Springer TA (2009) Mechanoenzymatic cleavage of the ultralarge vascular protein von Willebrand factor. *Science* 324:1330–1334.
8. Harrison-Lavoie KJ, et al. (2006) P-selectin and CD63 use different mechanisms for delivery to Weibel-Palade bodies. *Traffic* 7:647–662.
9. Hannah MJ, et al. (2003) Weibel-Palade bodies recruit Rab27 by a content-driven, maturation-dependent mechanism that is independent of cell type. *J Cell Sci* 116:3939–3948.
10. Knop M, Aareskjold E, Bode G, Gerke V (2004) Rab3D and annexin A2 play a role in regulated secretion of vWF, but not tPA, from endothelial cells. *EMBO J* 23:2982–2992.
11. Kobayashi T, et al. (2000) The tetraspanin CD63/lamp3 cycles between endocytic and secretory compartments in human endothelial cells. *Mol Biol Cell* 11:1829–1843.
12. Wagner DD, et al. (1991) Induction of specific storage organelles by von Willebrand factor propolypeptide. *Cell* 64:403–413.
13. Hoenger A, McIntosh JR (2009) Probing the macromolecular organization of cells by electron tomography. *Curr Opin Cell Biol* 21:89–96.
14. Leis A, Rockel B, Andrees L, Baumeister W (2009) Visualizing cells at the nanoscale. *Trends Biochem Sci* 34:60–70.
15. McIntosh R, Nicastro D, Mastronarde D (2005) New views of cells in 3D: An introduction to electron tomography. *Trends Cell Biol* 15:43–51.
16. Comolli LR, Downing KH (2005) Dose tolerance at helium and nitrogen temperatures for whole cell electron tomography. *J Struct Biol* 152:149–156.
17. Henderson GP, Gan L, Jensen GJ (2007) 3-D ultrastructure of O. tauri: Electron cryotomography of an entire eukaryotic cell. *PLoS One* 2:e749.
18. Grunewald K, Medalia O, Gross A, Steven AC, Baumeister W (2003) Prospects of electron cryotomography to visualize macromolecular complexes inside cellular compartments: Implications of crowding. *Biophys Chem* 100:577–591.
19. Koning RI, et al. (2008) Cryo electron tomography of vitrified fibroblasts: Microtubule plus ends *in situ*. *J Struct Biol* 161:459–468.
20. Medalia O, et al. (2002) Macromolecular architecture in eukaryotic cells visualized by cryoelectron tomography. *Science* 298:1209–1213.
21. Al-Amoudi A, et al. (2004) Cryo-electron microscopy of vitreous sections. *EMBO J* 23:3583–3588.
22. Gruska M, Medalia O, Baumeister W, Leis A (2008) Electron tomography of vitreous sections from cultured mammalian cells. *J Struct Biol* 161:384–392.
23. Valentijn KM, Valentijn JA, Jansen KA, Koster AJ (2008) A new look at Weibel-Palade body structure in endothelial cells using electron tomography. *J Struct Biol* 161:447–458.
24. Zenner HL, Collinson LM, Michaux G, Cutler DF (2007) High-pressure freezing provides insights into Weibel-Palade body biogenesis. *J Cell Sci* 120:2117–2125.
25. Huang RH, et al. (2008) Assembly of Weibel-Palade body-like tubules from N-terminal domains of von Willebrand factor. *Proc Natl Acad Sci USA* 105:482–487.
26. Henderson R (1995) The potential and limitations of neutrons, electrons and X-rays for atomic resolution microscopy of unstained biological molecules. *Q Rev Biophys* 28:171–193.
27. Grimm R, et al. (1998) Electron tomography of ice-embedded prokaryotic cells. *Biophys J* 74:1031–1042.
28. Koster AJ, et al. (1997) Perspectives of molecular and cellular electron tomography. *J Struct Biol* 120:276–308.
29. Dubochet J, Lepault J, Freeman R, Berriman JA, Homo J-C (1982) Electron microscopy of frozen water and aqueous solutions. *J Microsc* 128:219–237.
30. Matsui T, Titani K, Mizuochi T (1992) Structures of the asparagine-linked oligosaccharide chains of human Von Willebrand factor—occurrence of blood group A, Group B, and group H(O) structures. *J Biol Chem* 267:8723–8731.
31. Lui-Roberts WW, Collinson LM, Hewlett LJ, Michaux G, Cutler DF (2005) An AP-1/clathrin coat plays a novel and essential role in forming the Weibel-Palade bodies of endothelial cells. *J Cell Biol* 170:627–636.
32. Nightingale TD, Pattni K, Hume AN, Seabra MC, Cutler DF (2009) Rab27a and MyRIP regulate the amount and multimeric state of VWF released from endothelial cells. *Blood* 113:5010–5018.
33. Murk JL, et al. (2003) Influence of aldehyde fixation on the morphology of endosomes and lysosomes: Quantitative analysis and electron tomography. *J Microsc* 212:81–90.
34. Futter CE, Pearse A, Hewlett LJ, Hopkins CR (1996) Multivesicular endosomes containing internalized EGF-EGF receptor complexes mature and then fuse directly with lysosomes. *J Cell Biol* 132:1011–1023.
35. Eskelinen EL (2008) Fine structure of the autophagosome. *Methods Mol Biol* 445:11–28.
36. Michaux G, et al. (2006) The physiological function of von Willebrand's factor depends on its tubular storage in endothelial Weibel-Palade bodies. *Dev Cell* 10:223–232.
37. Fowler WE, Fretto LJ, Hamilton KK, Erickson HP, McKee PA (1985) Substructure of human von Willebrand factor. *J Clin Invest* 76:1491–1500.
38. Michaux G, Pullen TJ, Haberichter SL, Cutler DF (2006) P-selectin binds to the D'-D3 domains of von Willebrand factor in Weibel-Palade bodies. *Blood* 107:3922–3924.
39. Cohen AE, Mahadevan L (2003) Kinks, rings, and rackets in filamentous structures. *Proc Natl Acad Sci USA* 100:12141–12146.
40. Erent M, et al. (2007) Rate, extent and concentration dependence of histamine-evoked Weibel-Palade body exocytosis determined from individual fusion events in human endothelial cells. *J Physiol* 583:195–212.
41. Arvan P, Castle D (1998) Sorting and storage during secretory granule biogenesis: Looking backward and looking forward. *Biochem J* 332:593–610.
42. Thiele C, Huttner WB (1998) Protein and lipid sorting from the trans-Golgi network to secretory granules-recent developments. *Semin Cell* Dev Biol 9:511–516.
43. Arribas M, Cutler DF (2000) Weibel-Palade body membrane proteins exhibit differential trafficking after exocytosis in endothelial cells. *Traffic* 1:783–793.
44. Mastronarde DN (1997) Dual-axis tomography: An approach with alignment methods that preserve resolution. *J Struct Biol* 120:343–352.
45. Heymann JB, Cardone G, Winkler DC, Steven AC (2008) Computational resources for cryo-electron tomography in Bsoft. *J Struct Biol* 161:232–242.
46. Chen H, Hughes DD, Chan TA, Sedat JW, Agard DA (1996) IVE (Image Visualization Environment): A software platform for all three-dimensional microscopy applications. *J Struct Biol* 116:56–60.
47. Crowther RA, Henderson R, Smith JM (1996) MRC image processing programs. *J Struct Biol* 116:9–16.
48. Frank J, et al. (1996) SPIDER and WEB: Processing and visualization of images in 3D electron microscopy and related fields. *J Struct Biol* 116:190–199.
49. Egelman EH (2000) A robust algorithm for the reconstruction of helical filaments using single-particle methods. *Ultramicroscopy* 85:225–234.
50. Egelman EH (2007) The iterative helical real space reconstruction method: Surmounting the problems posed by real polymers. *J Struct Biol* 157:83–94.
51. Hannah MJ, et al. (2005) Differential kinetics of cell surface loss of von Willebrand factor and its propolypeptide after secretion from Weibel-Palade bodies in living human endothelial cells. *J Biol Chem* 280:22827–22830.